A Modeling Study of Typhoon Nari (2001) at Landfall. Part I: Topographic Effects

MING-JEN YANG

Department of Atmospheric Sciences, and Institute of Hydrological Sciences, National Central University, Chung-Li, Taiwan

DA-LIN ZHANG

Department of Atmospheric and Oceanic Science, University of Maryland, College Park, College Park, Maryland

HSIAO-LING HUANG

Institute of Hydrological Sciences, National Central University, Chung-Li, Taiwan

(Manuscript received 9 March 2007, in final form 21 February 2008)

ABSTRACT

Although there have been many observational and modeling studies of tropical cyclones, understanding of their intensity and structural changes after landfall is rather limited. In this study, several 84-h cloud-resolving simulations of Typhoon Nari (2001), a typhoon that produced torrential rainfall of more than 1400 mm over Taiwan, are carried out using a quadruply nested–grid mesoscale model whose finest grid size was 2 km. It is shown that the model reproduces reasonably well Nari's kinematic and precipitation features as well as structural changes, as verified against radar and rain gauge observations. These include the storm track, the contraction and sizes of the eye and eyewall, the spiral rainbands, the rapid pressure rise ($\sim$1.67 hPa h^{-1}) during landfall, and the nearly constant intensity after landfall. In addition, the model captures the horizontal rainfall distribution and some local rainfall maxima associated with Taiwan's orography.

A series of sensitivity experiments are performed in which Taiwan's topography is reduced to examine the topographic effects on Nari's track, intensity, rainfall distribution, and amount. Results show that the impact of island terrain on Nari's intensity is nearly linear, with stronger storm intensity but less rainfall in lower-terrain runs. In contrast, changing the terrain heights produces nonlinear tracks with circular shapes and variable movements associated with different degrees of blocking effects. Parameter and diagnostic analyses reveal that the nonlinear track dependence on terrain heights results from the complex interactions between the environmental steering flow, Nari's intensity, and Taiwan's topography, whereas the terrain-induced damping effects balance the intensifying effects of latent heat release associated with the torrential rainfall in maintaining the near-constant storm intensity after landfall.

1. Introduction

Although track forecasts of tropical cyclones (TCs) have improved considerably in the past two decades, little skill has been demonstrated in the prediction of intensity and intensity change as a TC nears landfall (McAdie and Lawrence 2000). Successful forecasts of changes in a TC's intensity depend on many factors and processes, such as vertical wind shear, moisture content of the storm environment, upper-level perturbations, sea surface temperature (SST) and the underlying oceanic mixed layer depth, latent heat release from TCs, and coastal surface conditions. The multiscale interactions of these processes pose a great challenge in modeling TCs because they require realistic initial and boundary conditions and demand accurate representations of many physical processes at different scales.

Liu et al. (1997) was the first to obtain a successful real-data explicit simulation of a TC, namely, Hurricane Andrew (1992), using the fifth-generation Pennsylvania State University–National Center for Atmospheric Research (PSU–NCAR) Mesoscale Model (MM5). The model reproduces well the hurricane track, intensity, and intensity change as well as the ra-

Corresponding author address: Dr. Ming-Jen Yang, Department of Atmospheric Sciences, National Central University, 300 Chung-Da Road, Chung-Li, 320, Taiwan.
E-mail: mingjen@ncu.edu.tw

DOI: 10.1175/2008JAS2453.1

dius of maximum winds (RMW), the hurricane eye and eyewall, and the spiral rainbands. A series of diagnostic analyses from this simulation (Liu et al. 1999; Zhang et al. 2000, 2001, 2002; Yau et al. 2004) were performed to investigate the kinematics, microphysics, thermodynamics, and small-scale wind streaks in the inner core regions, as well as the balanced and unbalanced flows. Their results demonstrate that if fine enough grid resolution, realistic physical parameterizations, and accurate initial vortex characteristics are incorporated into the model, a successful prediction of a TC's track, intensity, and inner-core and precipitation structures can be achieved, given proper large-scale conditions and SST fields. Subsequently, nonhydrostatic, cloud-resolving studies of TCs have become commonplace—for example, the simulations of Hurricane Bob (Braun and Tao 2000), Diana (Davis and Bosart 2001), and Bonnie (Rogers et al. 2003; Zhu et al. 2004; Braun 2006)—and have achieved a fair amount of success.

In this study, we wish to extend the previous studies by conducting a cloud-resolving simulation of Typhoon Nari (2001) occurring over the Northwest Pacific, but we will focus more on its landfalling characteristics as it moves across Taiwan. Most previous modeling efforts have focused on the oceanic portion of TCs' life cycles, whereas only few studies (e.g., Tuleya 1994) have examined the impact of land surface conditions on landfalling TCs. Therefore, the first objective of this study is to investigate whether or not the model could reproduce the kinematic and precipitation features of the landfalling storm from the given subtropical synoptic conditions, as verified against available radar and rain gauge observations.

Typhoon Nari is selected for this study because of its erratic movements, very long duration, and torrential rainfall over Taiwan. The associated strong winds and heavy rainfall caused 104 casualties and $140 million (U.S. dollars) in agricultural losses in Taiwan. Several studies have been carried out to address different aspects of the storm. For example, Sui et al. (2005) estimated the contribution of hydrometeor convergence to precipitation efficiency when Nari was still over the ocean. Huang et al. (2005) examined the forecast improvement of Nari's track and rainfall using assimilated Global Positioning System (GPS) occultation refractivity data. Li et al. (2005) used the MM5-simulated rainfall to drive a hydrological model and reproduced well the fast river runoff associated with Nari.

Although there have been many observational and modeling studies of oceanic TCs (e.g., Kurihara and Bender 1982; Willoughby et al. 1984a,b; Marks and Houze 1987; Houze et al. 1992; Liu et al. 1999; Rogers et al. 2003; Braun 2006), the detailed structural changes of TCs, especially the secondary circulations and precipitation structures, after landfall are still poorly understood. Thus, the second objective of this paper is to examine the three-dimensional (3D) kinematic and precipitation structures of the storm, with a focus on the terrain-induced structural changes after landfall.

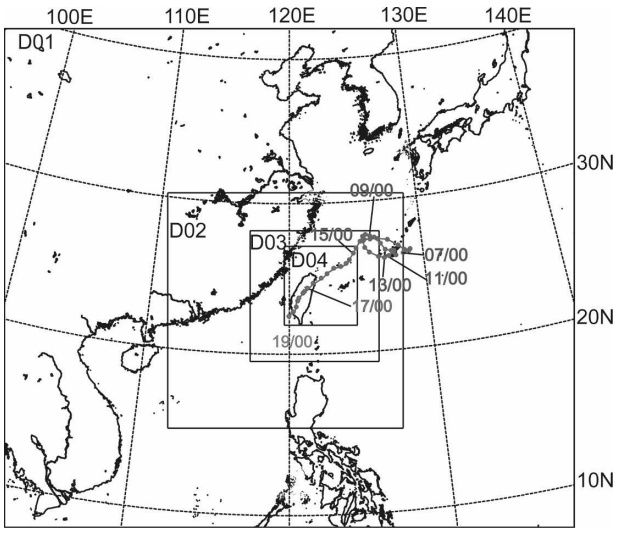

FIG. 1. The nested MM5 model domains, superposed with the 6-hourly best tracks of Typhoon Nari during its life cycle (i.e., from 0000 UTC 7 Sep to 0000 UTC 21 Sep 2001) issued by the CWB.

Assuming that an accurate track prediction could be obtained, the capability of a TC model to reproduce the rainfall distribution and amount of a landfalling TC may depend on the model's resolution of the storm circulations and terrain structures (Wu et al. 2002; Lin et al. 2002). Based on numerical experiments, Wu et al. (2002) indicated that the model and the terrain resolutions played equal roles in producing heavy rainfall over Taiwan's Central Mountain Range (CMR) for Typhoon Herb (1996). Therefore, the third objective of this study is to examine the topographic effects on the rainfall generation of Nari and its along-the-CMR track after landfall. This will be achieved through a series of terrain sensitivity experiments to be presented in section 6.

2. Overview

Because of its location in the northwest of the Pacific Ocean, Taiwan frequently suffers from disasters caused by landfalling TCs. In September, TCs usually move northwestward from the western Pacific Ocean to Taiwan and eastern China, and then curve northward to Korea and Japan (see Fig. 2 of Sui et al. 2002).

Figure 1 shows the best track of Typhoon Nari issued

by Taiwan's Central Weather Bureau (CWB) over the model-integration domain. It should be pointed out that the CWB's best track differs only slightly from that of the Joint Typhoon Warning Center (JTWC) for the oceanic portion prior to landfall, but it differs significantly after landfall. Because the CWB track includes real-time radar and surface observations over Taiwan, it should be more accurate than that of the JTWC and so it is used for the present study. The storm first appeared as a tropical depression on 6 September 2001. In the subsequent week (i.e., 7–13 September), Nari circled around (26°N, 126°E) as Typhoon Danas moved toward southern Japan on the east of Nari. After Danas moved eastward away from Japan on 12 September and a weak high pressure system developed over mainland China (near 30°N , 120°E), Nari began its southwestward movement, which deviated significantly from the usual northwestward track, toward Taiwan at a speed of 5–8 km h^{-1} (Figs. 2 and 3 and Table 1).

Typhoon Nari made landfall over Taiwan at 1300 UTC 16 September, and its eye shrank from 60 to 30 km in diameter with a maximum wind speed of 55 m s^{-1} (at an elevation of 2 km) as observed by the Next Generation Weather Radar (NEXRAD) installed on WuFeng Mountain (RCWF) over the northeastern coastal mountain (see Fig. 4 for the radar location). For the next three days (17–19 September), Nari moved across the CMR to western Taiwan and continued its southwestward path at a slow speed of 3–5 km h^{-1} along the west coast (Table 1 and Fig. 4). This is consistent with the weakening of the anticyclonic flow over mainland China (Figs. 2c,d), particularly with a decrease of the northeasterly steering flow to the north (Figs. 2b, 2d, and 3a). As Nari moved off Taiwan Island on 19 September, the low-level easterly flow to the east was intensified, thereby leading to an increase in the propagation of the storm (Figs. 2e,f and Table 1).

The evolution of the area-averaged environmental steering flow vectors (given in Fig. 3a) shows that initially Nari's steering flow is northeasterly to easterly. After Nari's landfall on Taiwan (1300 UTC 16 September), the environmental flow is less than 2 m s^{-1} because of the weakening of the high pressure system over China (Figs. 2c,d). Nari's propagation speed is less than the environmental steering flow speed after landfall (Table 1) as a result of the blocking and retardation by the terrain and surface friction. After 0000 UTC 18 September, the environmental flow changes to northeasterly, leading to the storm's southwestward movement.

Although Nari had only category 2 intensity on the Saffir–Simpson hurricane scale (Simpson 1974) prior to landfall and then quickly weakened to tropical-storm strength after landfall, the very long duration (53 h) of its slow passage across Taiwan Island (see Table 1 and Fig. 4) resulted in large quantities of accumulated rainfall. A 3-day (16–18 September) total rainfall of more than 1400 mm was observed over northern Taiwan, causing widespread flooding and severe mudslides and landslides.

3. Model description and initialization

A nonhydrostatic version of the PSU–NCAR MM5 model (version 3.5; Dudhia 1993; Grell et al. 1994) is used to simulate Typhoon Nari. The quadruply nested grid (54, 18, 6, and 2 km) domains are shown in Fig. 1 and their domain information is given in Table 2. There are 32 σ levels in the vertical for all four nested domains, with the model top set at 50 hPa and higher resolution in the planetary boundary layer (PBL).[1] The 54-, 18-, and 6-km grids are integrated in a two-way interactive mode for 84 h, starting at 1200 UTC 15 September and ending at 0000 UTC 19 September 2001. The 2-km grid is run separately for 84 h with initial and boundary conditions provided from the outputs of 6-km grid, mainly to increase computational efficiency in light of the numerous sensitivity experiments to be conducted. A comparative experiment with all four domains in a two-way interactive mode was conducted, and only minor differences were found.

The physics options used in the control simulation (CTL) include the Grell (1993) cumulus parameterization, the Reisner et al. (1998) microphysics scheme with graupel included, the Medium-Range Forecast (MRF) model PBL parameterization (Hong and Pan 1996), and the atmospheric radiation scheme of Dudhia (1989). No cumulus parameterization scheme is used for the 6- and 2-km grids, although some studies (e.g., Warner and Hsu 2000) suggest that excluding it on the 6-km grid may result in underprediction of rainfall. The initial and boundary conditions of the model integration are taken from the advanced global analysis of the European Center for Medium-Range Weather Forecasts (ECMWF)/Tropical Ocean Global Atmosphere (TOGA) data sets, at 1.125° × 1.125° horizontal resolution. The SST is kept constant during the model integration.

Because the typhoon vortex contained in the large-scale ECMWF/TOGA analysis is too weak and too broad, the TC initialization procedure of Davis and

[1] The 32 σ levels are located at 1, 0.997, 0.995, 0.992, 0.99, 0.985, 0.98, 0.975, 0.97, 0.965, 0.96, 0.95, 0.93, 0.9, 0.85, 0.8, 0.75, 0.7, 0.65, 0.6, 0.55, 0.5, 0.45, 0.4, 0.35, 0.3, 0.25, 0.2, 0.15, 0.1, 0.05, and 0.

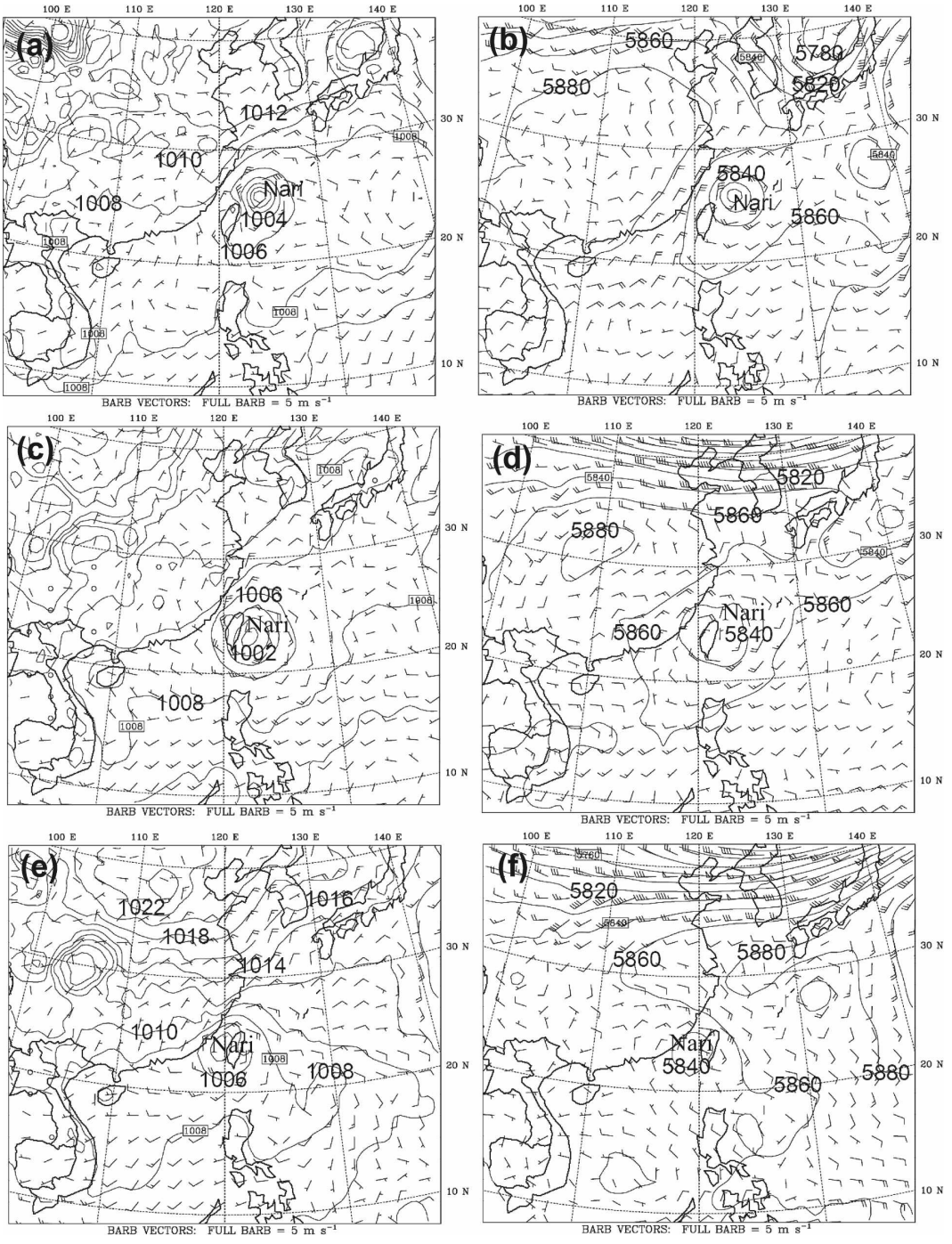

FIG. 2. Horizontal maps of (left) sea level pressure (every 2 hPa) and surface flow vectors and (right) geopotential height (every 20 m) and flow vectors at 500 hPa from the ECMWF–TOGA analysis at (a), (b) 1200 UTC 15 Sep, (c), (d) 0000 UTC 17 Sep, and (e), (f) 0000 UTC 19 Sep 2001, respectively.

Low-Nam (2001) is used to represent Nari's initial vortex. The erroneously broad vortex circulation in the large-scale analysis is first removed, and an axisymmetric Rankine vortex is then inserted into the horizontal wind field, with Nari's characteristics (i.e., 39 m s^{-1} of maximum wind and 50 km of RMW) estimated from the RCWF radar observation. The 3D axisymmetric tangential wind is constructed using a vertical weighting

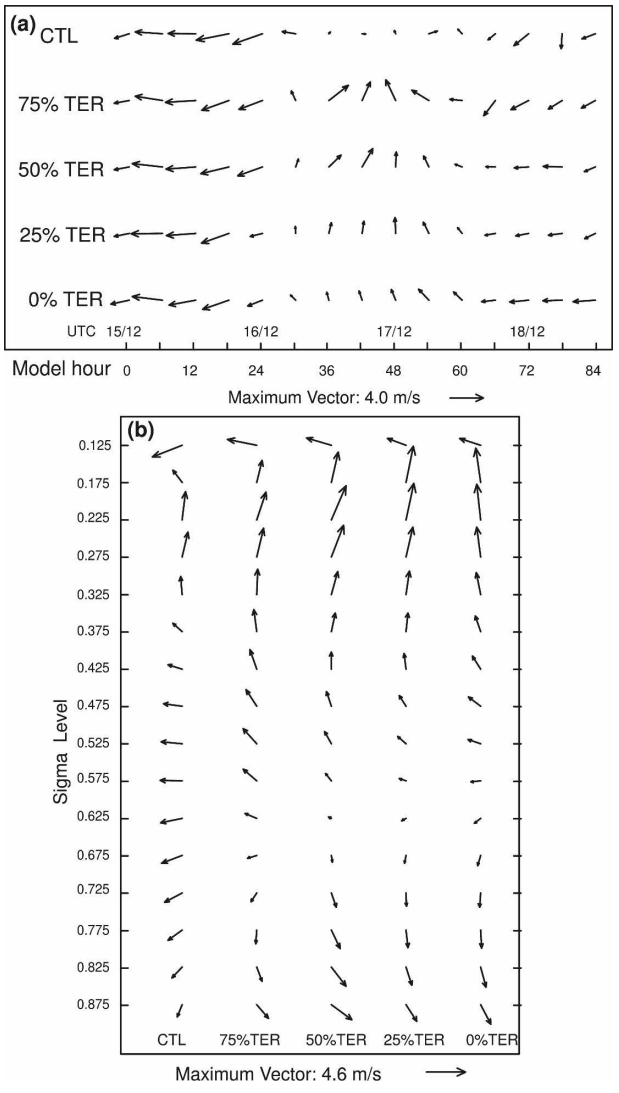

FIG. 3. (a) Environmental steering flow vectors from the control and terrain sensitivity experiments, calculated by averaging horizontally within a radius of 360 km from the simulated Nari and vertically between sigma levels of 0.9 and 0.1. (b) As in (a) but for vertical profiles (in sigma level) of environmental flows at 1800 UTC 16 Sep 2001.

function, which is specified as 0.99 from the surface through 950 hPa, 1.0 at 850 hPa, 0.97 at 700 hPa, 0.85 at 500 hPa, 0.6 at 300 hPa, 0.3 at 200 hPa, and 0.1 at 100 hPa. The nonlinear balance equation (Charney 1955) is

TABLE 1. Observed and simulated propagation speed (km h^{-1}) of Typhoon Nari at 12-h intervals.

Time	12 h	24 h	36 h	48 h	60 h	72 h	84 h
Date/UTC	16/00	16/12	17/00	17/12	18/00	18/12	19/00
Observed	6.3	9.9	12.2	4.3	3.6	3.4	8.3
Simulated	14.0	10.3	7.5	6.1	3.5	2.8	4.1

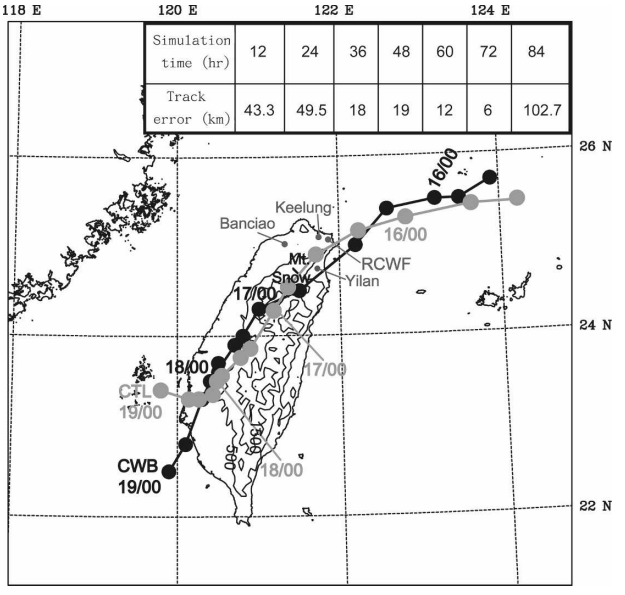

FIG. 4. Comparison of the CWB best track (CWB; thick solid) and the simulated track (CTL; gray solid) of Typhoon Nari, superposed with the terrain height (thin solid) at 1000-m intervals (starting at 500-m height). Each dot denotes Nari's central position every 6 h. The inset table is for the simulated track error with respect to the CWB analysis at 12-h intervals.

then used to obtain the 3D geopotential height field, and the hydrostatic equation is used to obtain the 3D atmospheric temperature. Moisture is assumed to be near-saturated in the vertical columns (with a relative humidity of 95% below 400 hPa, gradually reduced to 20% at the model top) within the RMW, smoothly merged with the environmental ECMWF/TOGA moisture value from the RMW to 200-km radius. The Rankine vortex is "relocated" in a position slightly (40 km) to the southeast of the reported position from the CWB best-track analysis to reproduce Nari's landfalling location and capture the subsequent landfalling characteristics as observed.

4. Model verification

In this section, we will verify the control simulation against various observations, such as best-track estimates, rain gauge data, and radar analyses.

a. Track and intensity

Figure 4 compares the model-simulated track of Nari to the CWB best-track estimates, using results from the 6-km, larger-scale domain. In general, the MM5 simulates Nari's track very well, especially its landfall near Yilan at 22 h into the integration (valid at 1000 UTC 16 September, henceforth 16/10–22), albeit 3 h earlier than

TABLE 2. The model design.

Domain	D1	D2	D3	D4
Dimensions (x, y)	81 × 71	100 × 100	166 × 166	271 × 301
Grid size (km)	54	18	6	2
Area coverage (km × km)	4320 × 3780	1782 × 1782	990 × 990	540 × 600
Time step (s)	90	30	10	3.3
Integration hours	0–84	0–84	0–84	0–84

and 20 km to the north of the observed. Note that because of the landfall timing error, some model results will be verified when the simulated and observed storms are closely located but with timing errors. The model also reproduces reasonably well the relatively fast and slow passage of Nari from northeast to southwest across Taiwan before and after 17/00–36, respectively (Table 1). However, the simulated track begins to deviate from the observed after 18/12–72, leading to large displacement errors at the end of the 84-h integration.

Figure 5 shows that the 2-km simulated storm intensity prior to landfall, indicated by the minimum sea level pressure of 941 hPa and the maximum surface wind of 50 m s^{-1}, is stronger than that of the best-track estimates (960 hPa and 40 m s^{-1}). During landfall, the simulated storm compares favorably to the best-track estimates for Nari's minimum central pressure decrease (at a rate of 1.67 hPa h^{-1}) and maximum surface wind weakening (at a rate of 1 m s^{-1} h^{-1}) over 24 h. Of interest is that both the observed and simulated storms remain at nearly constant intensities for 36 h after passing the CMR. This differs from the typical landfall characteristics in that landfalling TCs tend to experience continuous weakening while moving farther inland. To our knowledge, in the past 20 yr, only 4 TCs (including Nari) maintained constant intensities during their landfalls over Taiwan. The near-constant intensity of Nari during its landfall will be discussed in section 5.

b. Accumulated rainfall

Figures 6a, 6b, and 6c compare the simulated 24-h accumulated rainfall on 16, 17, and 18 September 2001 to the rain gauge observations, respectively; Fig. 7 compares the 3-day rainfall totals over Taiwan. On 16 September, Typhoon Nari brought torrential rainfall into northern Taiwan (Fig. 6a). Subsequently, Nari was hindered by the CMR's steep terrain and moved very slowly southwestward (Fig. 4); this slow motion aggravated the accumulation of heavy precipitation. The interaction of Nari's circulation (northeasterly and easterly) with local concave topography over the northeastern Taiwan gave rise to a 24-h maximum rainfall amount of 1189 mm over Mt. Snow on 17 September (Fig. 6b). When Nari moved to the southwestern coastal region on 18 September, intense convection in the inner-core region produced a local rainfall maximum of 523 mm at the foothill of the CMR (Fig. 6c). The 3-day (from 16/00–12 to 19/00–84) rainfall totals are given in Fig. 7a, which shows the generation of 1431 mm over Mt. Snow and 1241 mm at the southwestern foothills of the CMR.

It is evident that the model captures the rainfall distribution and some local rainfall maxima, except for the observed coverage of light rainfall in the central CMR (Figs. 6b and 7). Part of this difference in the light rainfall coverage appears to result from the lack of rain gauge stations along the CMR's ridges (see Chien et al. 2002 or Yang et al. 2004 for the distribution of the rain gauge network) because radar data does indicate precipitation signatures over the region (Fig. 8). As for the rainfall intensity, we see that the 6- and 2-km grids simulate 24-h rainfall maxima of 673 and 889 mm, re-

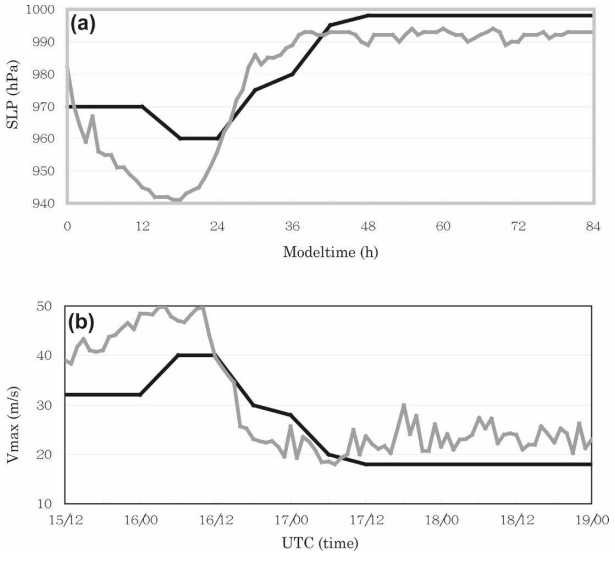

FIG. 5. Time series of (a) the minimum sea level pressure (SLP; in units of hPa) and (b) the surface maximum wind (V_{max}; in units of m s^{-1}) from the 6-hourly CWB best track analysis (dark solid) and the hourly 2-km CTL simulation (gray) during the period of 1200 UTC 15 Sep to 0000 UTC 19 Sep 2001.

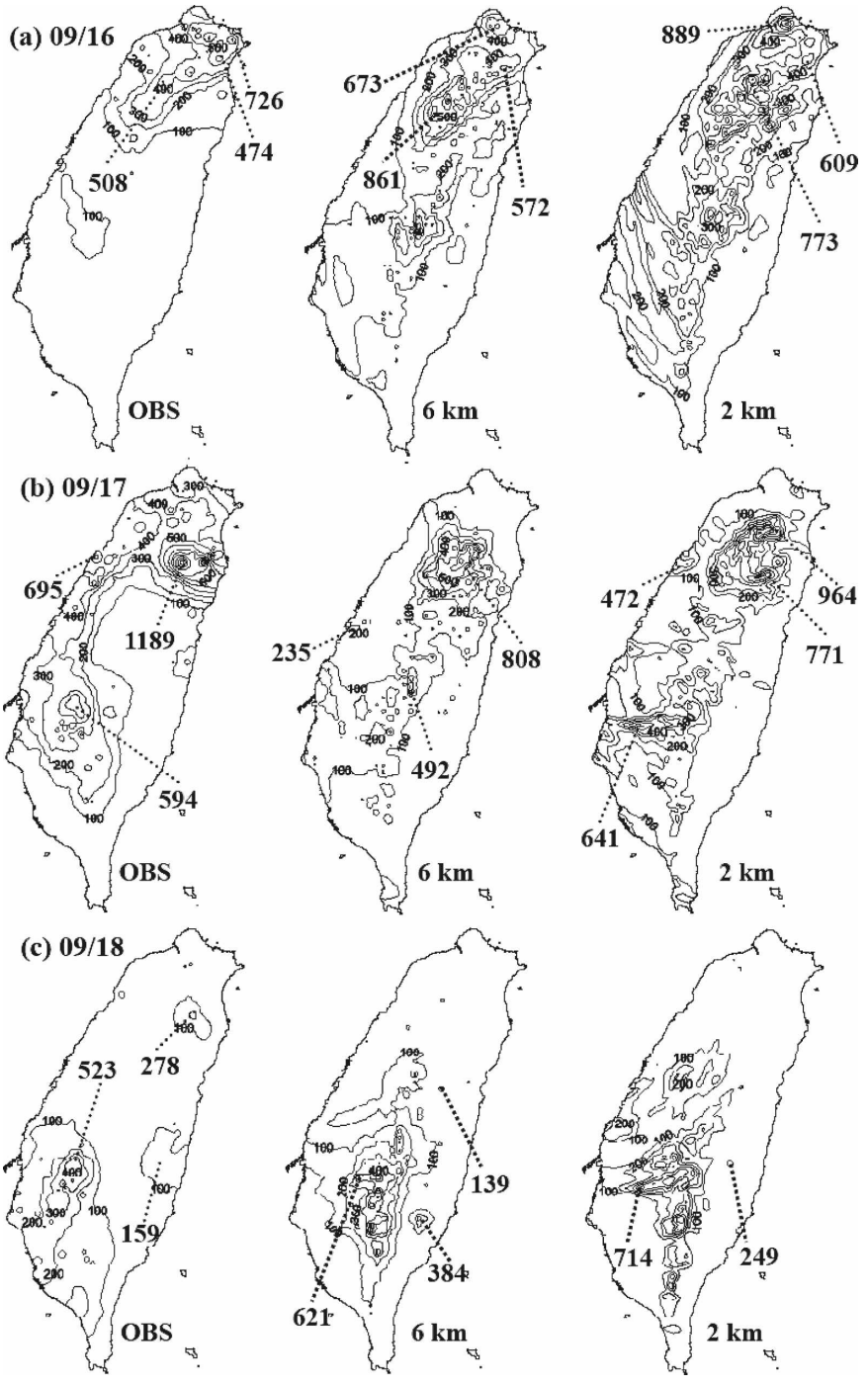

FIG. 6. Horizontal maps of the 24-h accumulated rainfall at intervals of 100 mm over Taiwan from the (left) observations, (middle) 6-km grid, and (right) 2-km grid during (a) 16–17 Sep, (b) 17–18 Sep, and (c) 18–19 Sep 2001. All time periods begin and end at 0000 UTC.

spectively, over northeastern Taiwan, where the observed 24-h rainfall maximum is 726 mm on 16 September (Fig. 6a). Clearly, the higher the horizontal resolution for topography and circulation, the more intense rainfall could be expected. On 17 September, however, the 6- and 2-km grids produce local rainfall maxima of 808 and 964 mm, respectively, which are both less than the rain gauge–observed 1189 mm over Mt. Snow (Fig. 6b). This rainfall underprediction may be caused partly by not fine enough resolution and partly by the 20-km

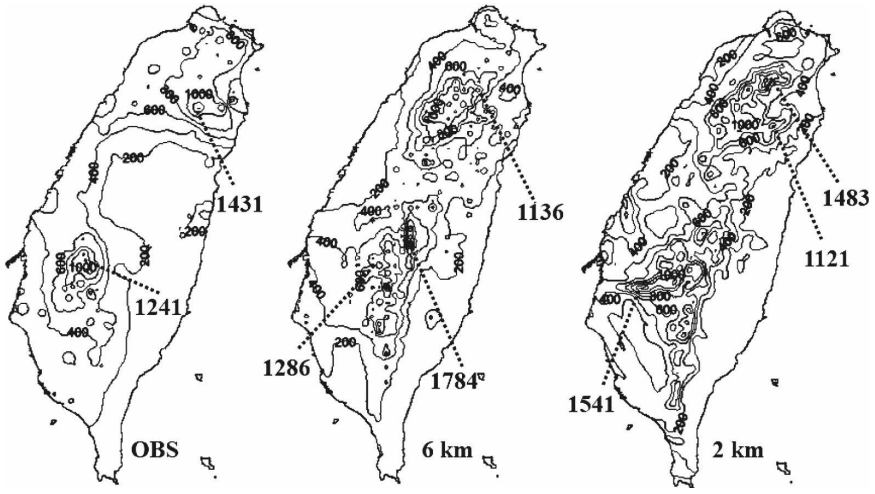

FIG. 7. As in Fig. 6, but for the 72-h accumulated rainfall during the period of 0000 UTC 16–19 Sep 2001. Contour interval is 200 mm.

position error at landfall, during which period the inner-core dynamical forcing may not be in a favorable phase with topographical lifting. On 18 September, both the 6- and 2-km grids simulate more rainfall at the southwestern foothills of the CMR, as compared to the observations (Fig. 6c).

For the accumulated total rainfall during the passage of Nari, Fig. 7 shows that both 6- and 2-km grids reproduce reasonably well the observed 3-day total rainfall maxima over Mt. Snow and the southwestern foothill of the CMR, although the extreme values at the mountain peaks from the 2-km grid are higher than the rain gauge observed. The simulated 3-day rainfall pattern over the central CMR also appears to be realistic when the radar echoes along the CMR ridges are taken into account.

To further examine the model performance in simulating Nari's rainfall on Taiwan, Fig. 9 compares the distribution of the simulated 72-h rainfall to the observed. It is evident that the CTL simulation tends to overpredict the occurrence distribution (or area coverage) of 3-day rainfall totals less than 550 mm but underpredict that of more than 550 mm. This appears to be a common feature of a mesoscale model (i.e., Colle et al. 1999; Chien et al. 2002; Yang et al. 2004). With the grid refinement from 6 to 2 km, the spectrum of the simulated rainfall approaches the observed. On average, the simulated 3-day total rainfall from the 6- and

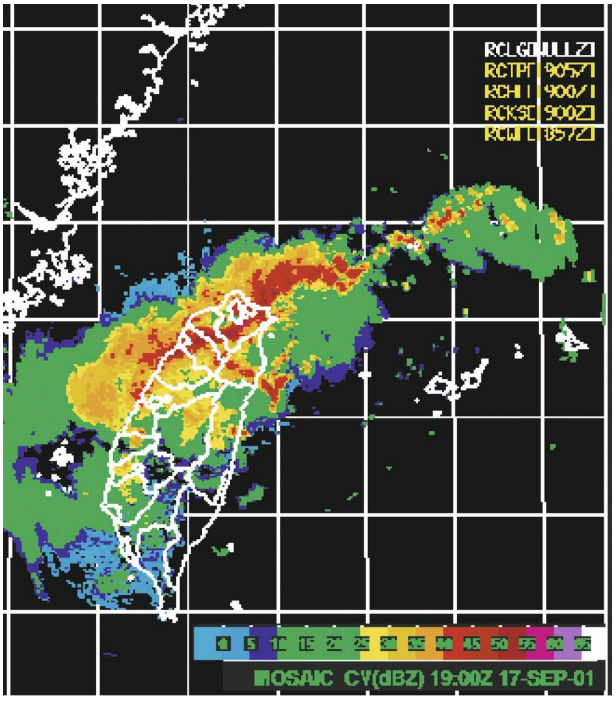

FIG. 8. A composite of vertical maximum radar reflectivity (colored) at 1900 UTC 17 Sep 2001.

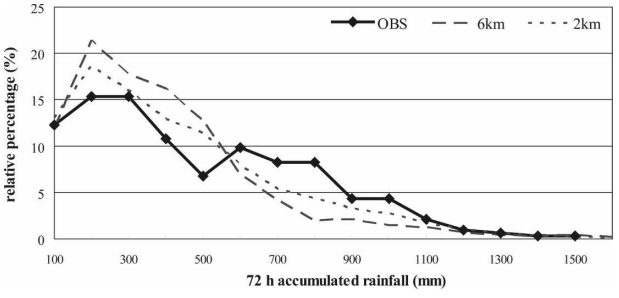

FIG. 9. The distribution of the 72-h accumulated rainfall amount (mm) relative to the total data points over Taiwan Island from the 6-km grid (long dashes), 2-km grid (short dashes), and the rain gauge observation (OBS; solid line) during 16–18 Sep 2001.

TABLE 3. The 72-h accumulated rainfall (mm) averaged over Taiwan Island on 16–18 Sep 2001.

Variable	OBS	6-km grid	2-km grid
Island-averaged rainfall (mm)	434.6	348.1	383.4
Percentage with respect to OBS (%)	100	80.1	88.2
Number of data points	325	1073	9602

2-km grids reaches 80% and 88% of the rain gauge observed amount, respectively (see Table 3). The results reveal that as the grid resolution increases, the model could better capture the statistical spectrum of accumulated rainfall. This is consistent with the finding of Wu et al. (2002) that the ability of a TC model to reproduce the observed rainfall of Typhoon Herb improves with refined horizontal resolutions. Thus, we may hypothesize that both the terrain and model grid resolutions play important roles in determining the predictability of rainfall amounts along the CMR in both (and other) typhoon cases.

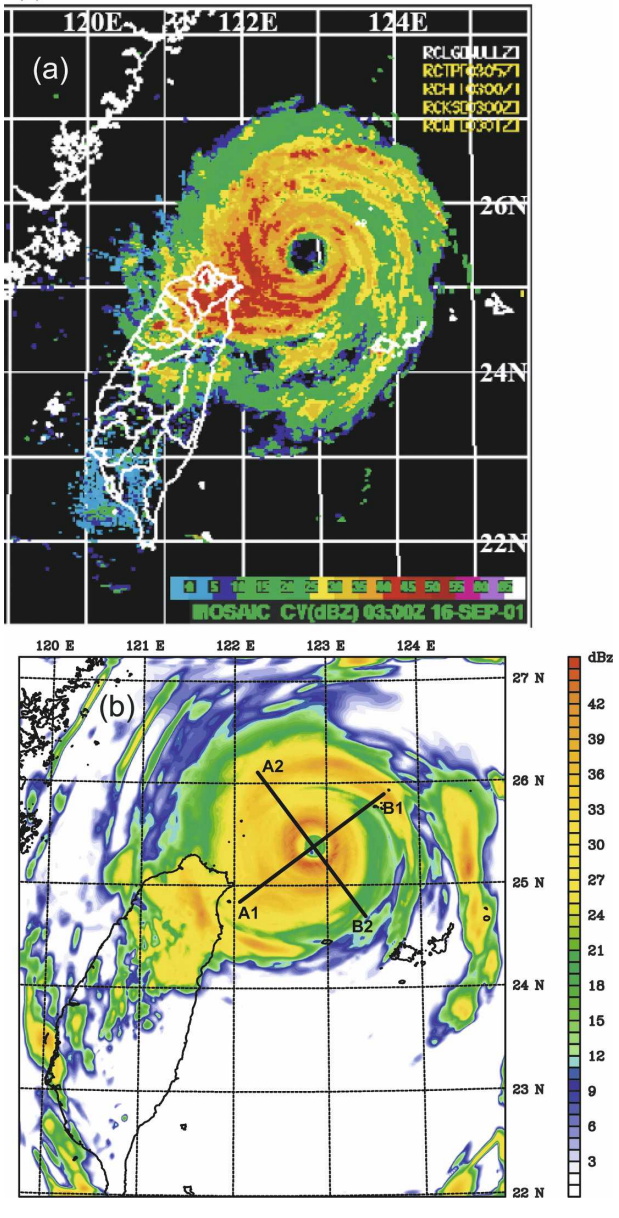

FIG. 10. (a) CV radar reflectivity (dBZ) at 0300 UTC 16 Sep 2001 and (b) the 1-h averaged radar reflectivity CV from the 2-km control simulation centered at 0130 UTC 16 Sep 2001. Lines A_1B_1 and A_2B_2 denote the locations of along-track and cross-track vertical cross sections, respectively.

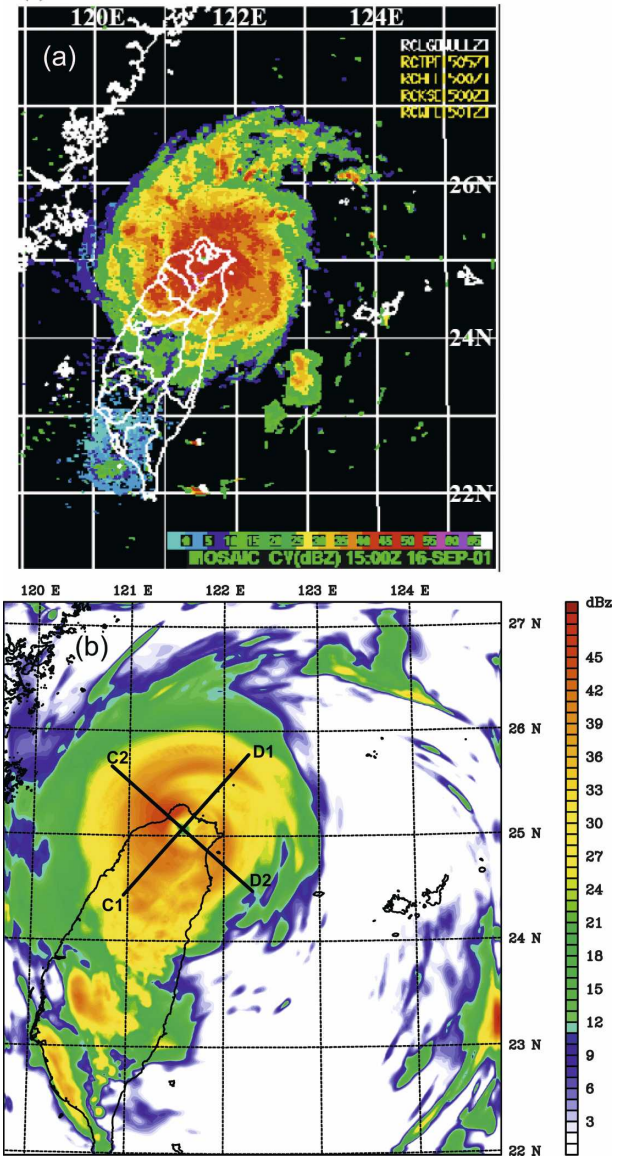

FIG. 11. As in Fig. 10, but for (a) the observation at 1500 UTC 16 Sep 2001 and (b) the 1-h averaged simulation result centered at 1200 UTC 16 Sep 2001. Lines C_1D_1 and C_2D_2 denote the location of along-track and cross-track vertical cross sections, respectively.

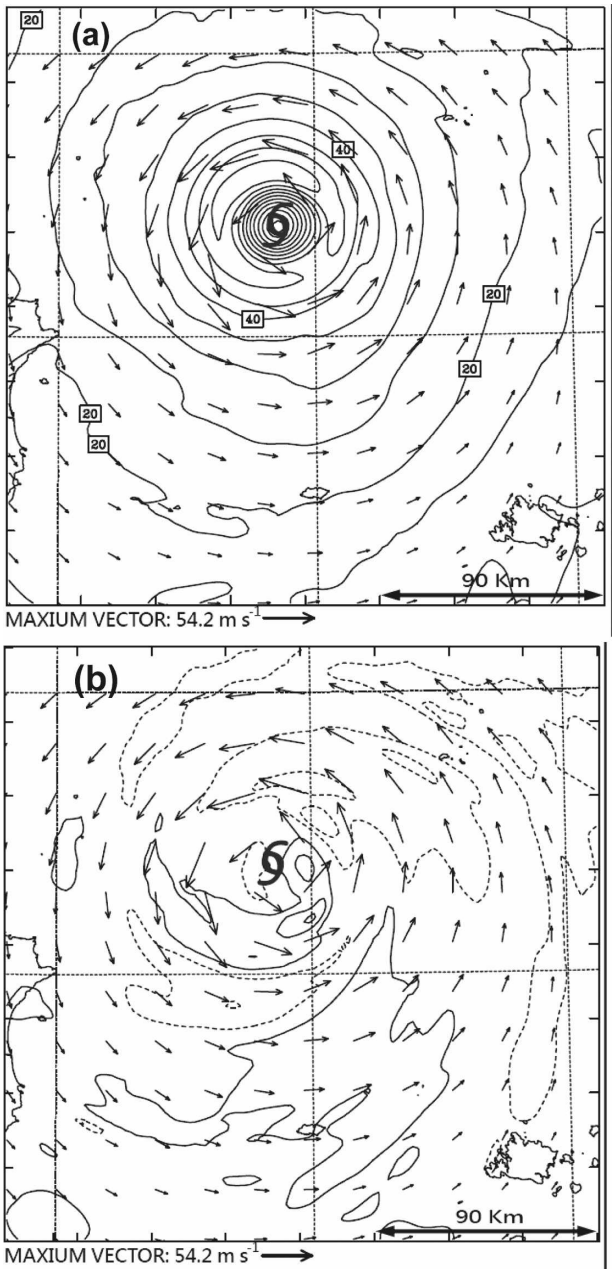

FIG. 12. Simulated 1-h averaged storm-relative (a) tangential (contoured every 5 m s^{-1}) and (b) radial wind fields (contoured every 2 m s^{-1}; solid line for radial outflow and dashed line for radial inflow) of Nari at 3 km AGL on the 2-km grid centered at 0130 UTC 16 Sep 2001. Superposed are the horizontal wind vectors (plotted every 5 grid points) at the 3-km level. The zero contour for radial wind in (b) is omitted. The TC symbol indicates the eye location.

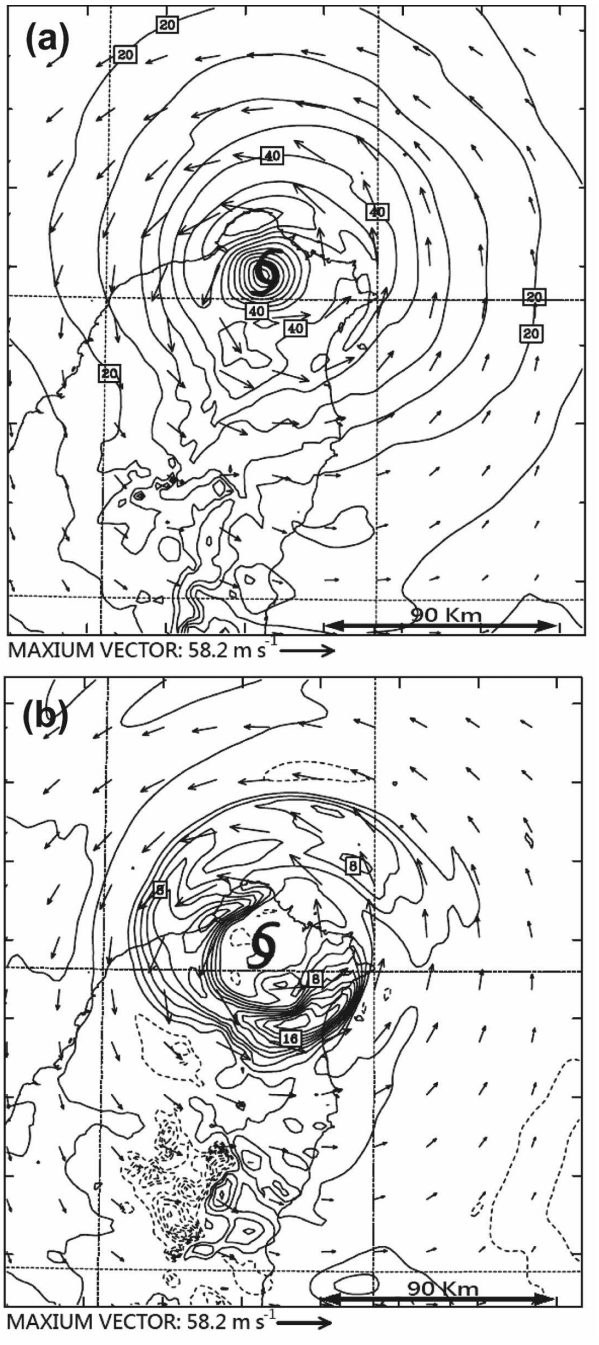

FIG. 13. As in Fig. 12, but for the 1-h averaged simulated storm-relative (a) tangential and (b) radial wind fields centered at 1200 UTC 16 Sep 2001.

c. *Horizontal storm structure*

Figures 10 and 11 compare the simulated vertical maximum radar reflectivity composite (CV) of Nari to the observed prior to and after landfall, respectively. The simulated radar reflectivity is calculated from the mixing ratios of rainwater, snow, and graupel, following Fovell and Ogura (1988), and then composited by averaging the 2-km model outputs at 2-min intervals for a 1-h period. Note that the observed radar CV maps in Figs. 10a and 11a are the only radar data to show the

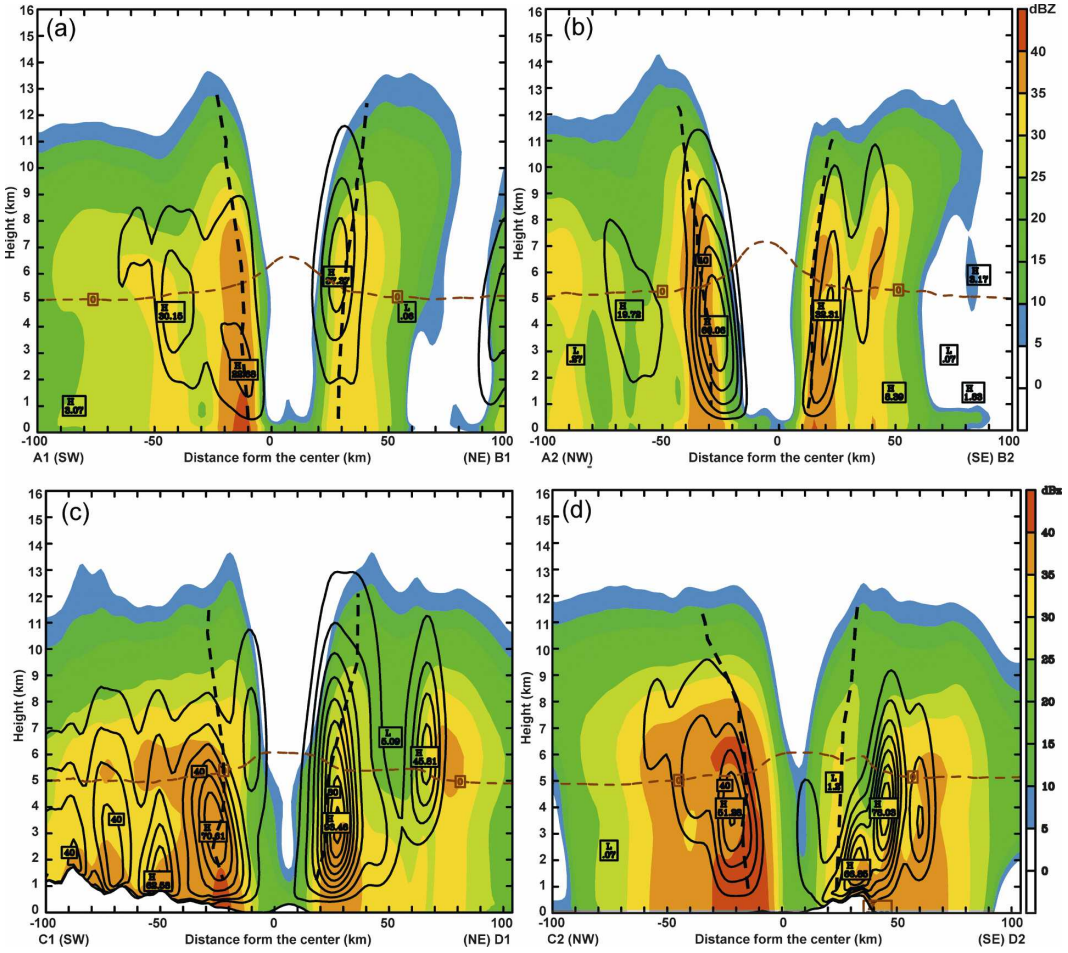

FIG. 14. (a) Along-track and (b) cross-track vertical cross sections of the 1-h averaged radar reflectivity (colors) and condensational heating rates (every 10 K h^{-1}) on the 2-km grid that is taken along line A_1B_1 and A_2B_2 in Fig. 10b from the 13–14-h simulations, centered at 0130 UTC 16 Sep 2001. (c), (d) As in (a), (b), but taken along line C_1D_1 and C_2D_2 in Fig. 11b from the 23.5–24.5-h simulations, centered at 1200 UTC 16 Sep. Dashed lines denote the 0°C isotherm; heavy dashed lines denote the vertical axis of RMW.

gross precipitation features of Nari over the whole island. Nari exhibited clearly near-axisymmetric eyewall structures when it was over the ocean, with more extensive precipitation coverage to the northern tip of Taiwan Island (Fig. 10a). The model reproduces well the axisymmetric eyewall and spiral rainbands (Fig. 10b), particularly the rainband that produced heavy rainfall over northern Taiwan.

It is evident from Fig. 11 that both the observed and simulated storms exhibit the absence of the echo-free eye after landfall and that their precipitation structures become more asymmetric, particularly for the eyewall on the eastern side of the CMR. One may note, however, that the model produces enhanced rainfall over the central CMR that is less obvious in the observation. This may be attributed partly to the removal of ground clutter in processing radar data and partly to the blocking of radar beams over high-terrain regions.

5. Structural changes prior to and after landfall

After validating the model simulations with available observations, it is desirable to gain insight into the 3D structural changes of Nari prior to and after landfall. To remove small-scale and transient variations, the simulation results are composited by averaging the instantaneous model outputs at 2-min intervals for a 1-h period (Figs. 12–16). Figure 12 shows that when Nari is over the ocean, its storm-relative tangential velocity exhibits a wavenumber-1 signature with a maximum speed near 55 m s^{-1}, whereas the radial velocity clearly has an asymmetric structure. The radial outflow in the southern eyewall suggests that the local strong tangential flow may be supergradient (Zhang et al. 2001). Two hours after landfall, Nari's tangential wind becomes highly asymmetric as a result of enhanced convergence and divergence induced by the local topography

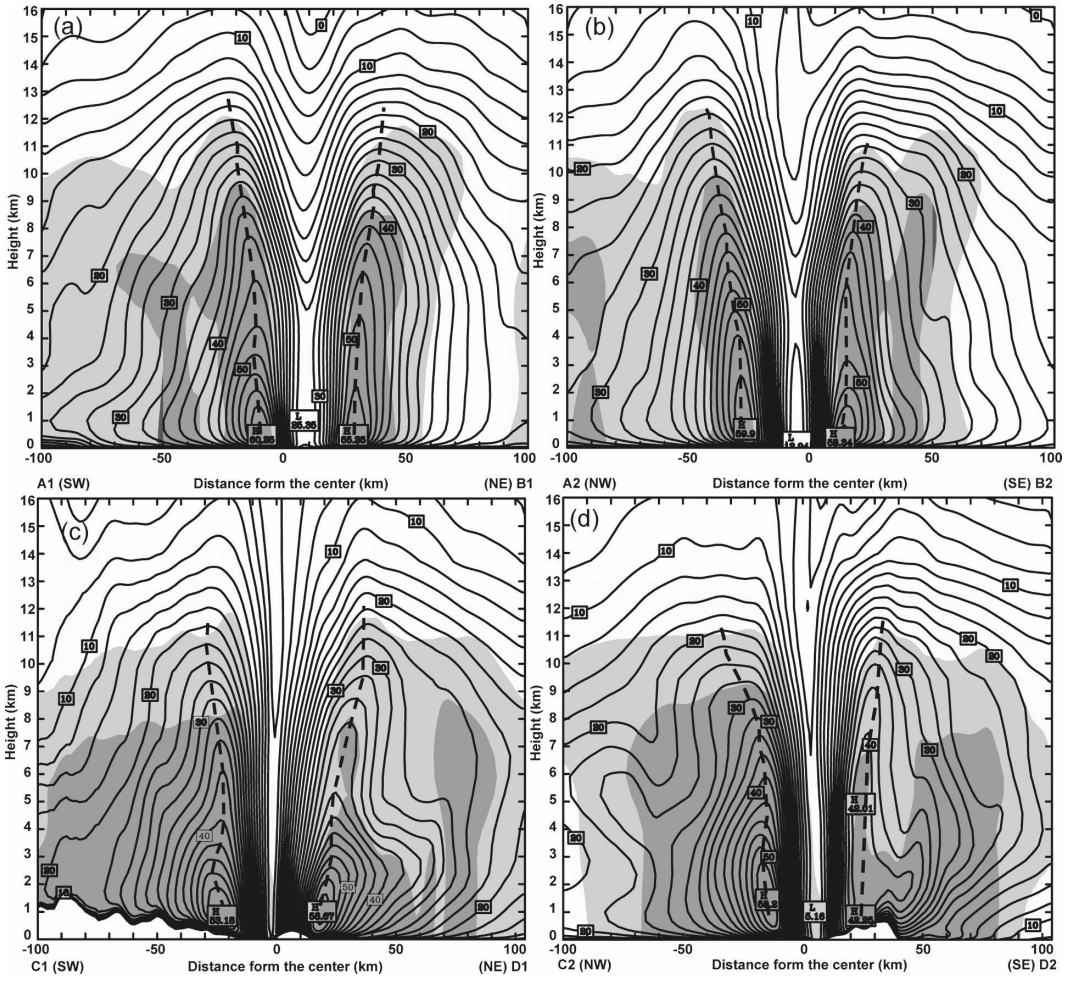

FIG. 15. As in Fig. 14, but for the storm-relative tangential winds (every 2.5 m s^{-1}). Solid (dashed) lines denote cyclonic (anticyclonic) winds. Dark and light gray shadings are for reflectivity greater than 30 dBZ and in the range of 15 and 30 dBZ, respectively. Heavy dashed lines denote the vertical axis of the RMW.

(Fig. 13a). The simulated radial wind in Fig. 13b exhibits many high wavenumber variations associated with flows over the hills and valleys in the CMR. It is significant that most portions of the radial flows are outward, implying that the local topography-induced secondary circulations tend to damp the typhoon vortex, as can be further seen in the vertical cross sections that follow.

Figures 14–16 show along-track and cross-track vertical cross sections of the condensational heating rates, tangential winds, and radial winds, respectively, superposed with the radar reflectivity. It is apparent from Figs. 10b and 14a,b that prior to landfall, the simulated storm exhibits upright precipitation structures below the melting level but outward-tilted ones above it, with more intense condensational heating in the northwestern quadrant. The latent heating rates show significant asymmetries in the vertical cross sections in spite of the near-axisymmetry in the radar reflectivity (cf. Figs. 10b and 14a,b). In addition, Nari's eye size, estimated by the 10-dBZ reflectivity contour, ranges from 25 km in diameter in the PBL to 50 km aloft (near the 12-km altitude).

After landfall, the northeast portion of the eyewall remains upright, whereas the southwestern eyewall appears to be "collapsed" over Mt. Snow, with greater precipitation width represented by radar reflectivity and latent heating (Fig. 14c). Significantly, after landfall both the local radar echo intensity and latent heating rate increase, particularly in the lower troposphere (cf. Figs. 14c,d). Moreover, the levels of maximum heating are located at a lower altitude with a significant increase in the local heating rate over terrain. Similar orographic features were also noted by Wu et al. (2002) in their numerical study of the landfall of Typhoon Herb (1996) over Taiwan and by Medina and Houze (2003) in their radar data analysis of orographically

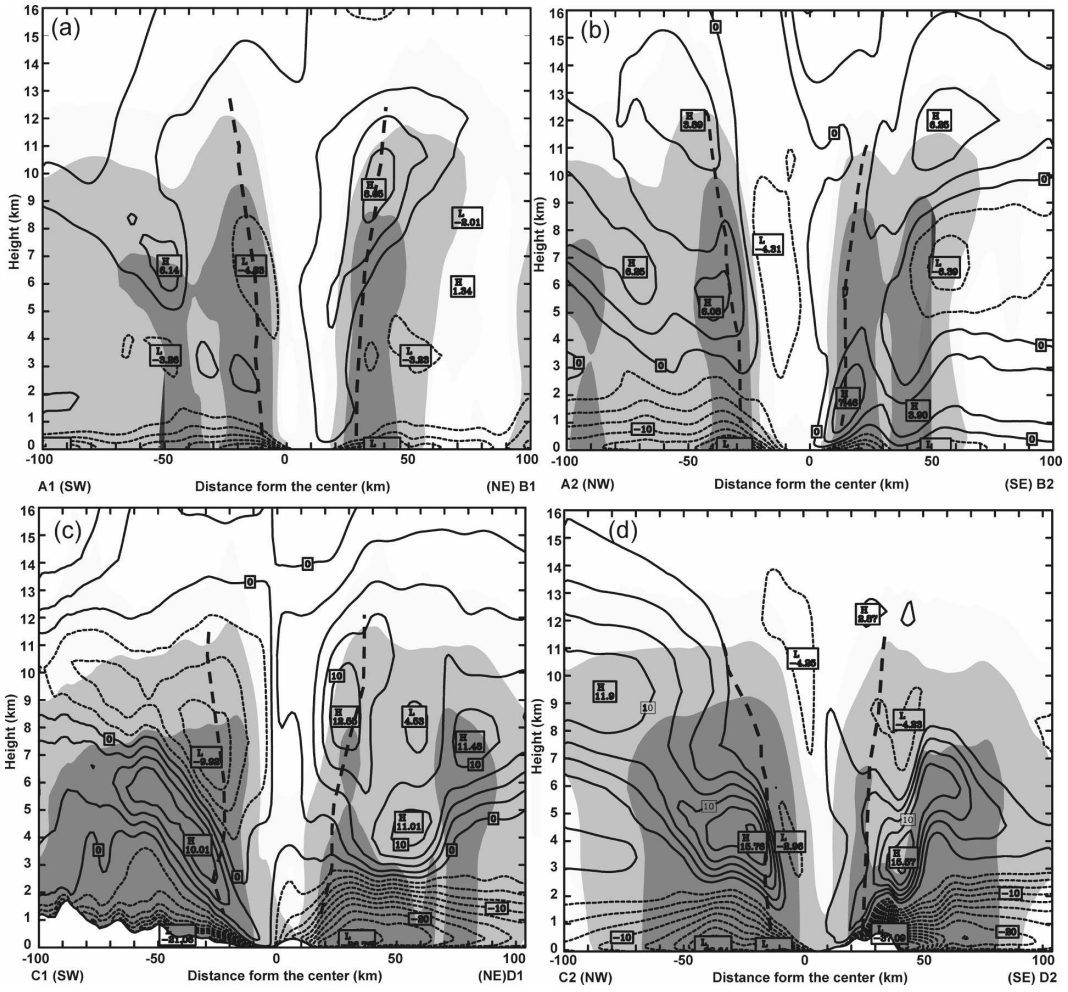

FIG. 16. As in Fig. 15, but for the storm-relative radial winds (every 2.5 m s^{-1}). Solid (dashed) lines are for radial outflow (inflow) speeds.

driven precipitation associated with Alpine convective storms. Of further importance is the fact that the typhoon eye nearly vanishes after landfall (Figs. 11b and 14c,d), likely as a result of the increased low-level radial inflows (Figs. 16c,d) and the orographically generated clouds and precipitation in the eye (Zhang and Kieu 2006).

Vertical structures of the tangential wind prior to landfall are similar to those in the previous studies of oceanic TCs (Jorgensen 1984; Marks and Houze 1987; Liu et al. 1997), with the peak winds near 60 m s^{-1} at the top of PBL (about 1 km AGL) on both sides of the eyewall (Figs. 15a,b). Unlike in the simulation of Hurricane Andrew (1992) by Liu et al. (1997), however, Nari's RMW shows little vertical tilt in the lower half of the troposphere, which is likely due to the different intensities between the two storms.

The previously mentioned asymmetric structures after landfall are also evident in the vertical structures of tangential winds, including the distribution of rotational flow gradients and the RMW (Figs. 15c,d). In addition, the RMW tilts toward Mt. Snow until 3 km AGL, indicating the important topographical effects on the TC's rotational flow structures (Fig. 15c).

The radial flow field shows an intense inflow in the PBL, with a peak value of 10–16 m s^{-1} near the ocean surface, and an outflow layer above, although it is relatively weak in the outer region in the northwestern quadrant (Figs. 16a,b). The paired inflow–outflow layers, driven by both the surface friction and latent heating, are typical of features found in many oceanic TCs (e.g., Jorgensen 1984; Marks and Houze 1987; Liu et al. 1999). As shown in Zhang et al. (2001) and Yau et al. (2004), the development of radial inflows and outflows determines the local spinup or spindown of a TC's primary circulations. Interestingly, the simulated Nari also

shows another paired inflow–outflow layer aloft that coincides with the midlevel latent heating maximum in the southeastern quadrant of the eyewall (cf. Figs. 14b and 16b).

After landfall, the simulated Nari exhibits increased radial inflows (stronger than 21 m s^{-1}) in the PBL due partly to the increased surface friction and partly to the enhanced latent heating in the lower troposphere (cf. Figs. 14c and 16c). The inflow layer in the northeastern quadrant extends to 5 km AGL at a 100-km radius in response to the pronounced latent heating above the melting level. In contrast, an intense sloping outflow jet as strong as 10 m s^{-1} develops above Mt. Snow, indicating that the strong tangential flow above the sloping topography is highly supergradient, as mentioned earlier. This topography-induced intense radial outflow may contribute to the spindown of the typhoon vortex, like the Ekman pumping (see section 5.4 of Holton 2004; Zhang and Kieu 2006). Similarly, the damping effects of the CMR on the vortex flows occur through the lower tropospheric spindown by increased radial outflows, as can also be seen in Fig. 13b. This helps explain the persistence of the strong rotational flow below 5 km over the mountain range despite the intense latent heat released from the heavy rainfall (cf. Figs. 15c and 16c).

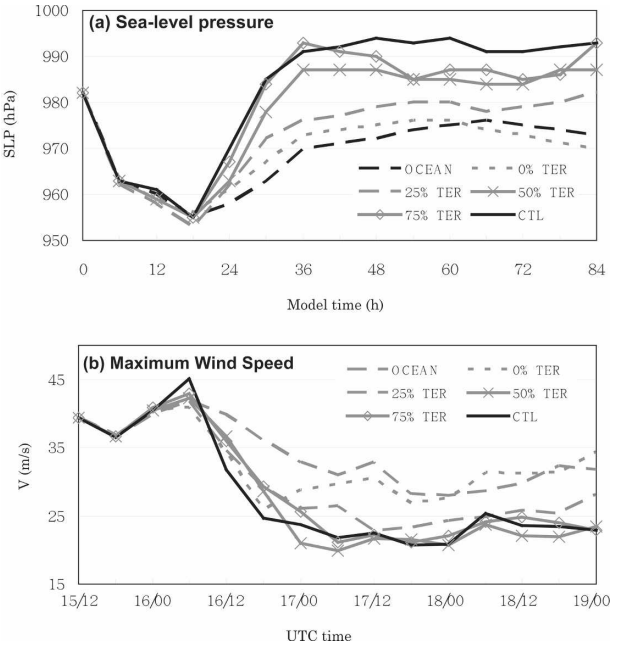

FIG. 17. As in Fig. 5, but for the sensitivity simulations to reduced terrain heights using 75%, 50%, 25%, and 0% of the terrain (TER) height field and ocean condition (OCEAN) in the control run. The 6-km control simulation (CTL) is also shown.

6. Terrain sensitivity experiments

In section 4b, we have shown pronounced correlations between Nari's rainfall distribution and Taiwan's topography (e.g., in Figs. 4, 6, and 7). Similar results were also shown by Wu et al. (2002) in their simulation of Typhoon Herb, but they concluded that the CMR had minor effects on Herb's track. Unlike Nari, Herb was a fast-moving, nearly category 5 typhoon, and it moved across Taiwan in 6 h. Hence, we hypothesize that the effects of local topography on the landfalling characteristics of Nari must differ substantially from those of Herb. To validate this hypothesis, five sensitivity experiments are conducted, in which all model parameters are held the same as those in the CTL simulation except that 75%, 50%, 25%, and 0% of Taiwan terrain elevations are used, respectively, plus one experiment with ocean conditions over Taiwan. For the volume originally occupied by the terrain, the atmospheric conditions are first created by vertically extrapolating ECMWF–TOGA analyses to the model ground and then blending them with the upper-air sounding and station observations through MM5's standard preprocessing package.

a. Track and intensity

It is apparent from Figs. 17 and 18 that the intensity of the simulated Nari responds linearly to the changes of Taiwan's topography, but its track responds in a complex manner. Specifically, the lower Taiwan's terrain height, the deeper the central pressure, and the stronger the maximum surface wind after landfall. As the terrain heights reduce to zero, Nari's intensity grows, central minimum pressure deepens by 15 hPa, and maximum surface wind increases by 6–7 m s^{-1} at 17/12–48, when the simulated storm is fully adjusted to the low-level conditions (Figs. 17a,b). The storm intensity of the ocean run is slightly stronger than that of the no-terrain run, owing to the extra contribution of sensible and latent heat fluxes from the ocean surface. The storm intensities of the no-terrain and ocean experiments increase after 18/00–60, when the simulated storms are displaced into the Taiwan Strait (Fig. 18d).

In contrast, reducing Taiwan's terrain height causes quite irregular changes to the storm track. That is, with the reduced topography, the simulated storms with stronger intensities move faster than the CTL storm as they approach northern Taiwan under the influence of the easterly steering flows (cf. Figs. 18 and 3a). Moreover, stronger storms tend to track more along the east coast immediately after landfall (16/09–21 to 16/21–33) because they experience more steering by the upper-level flows (cf. Figs. 3b and 18). Of interest is that during their southwestward journeys, the reduced-terrain

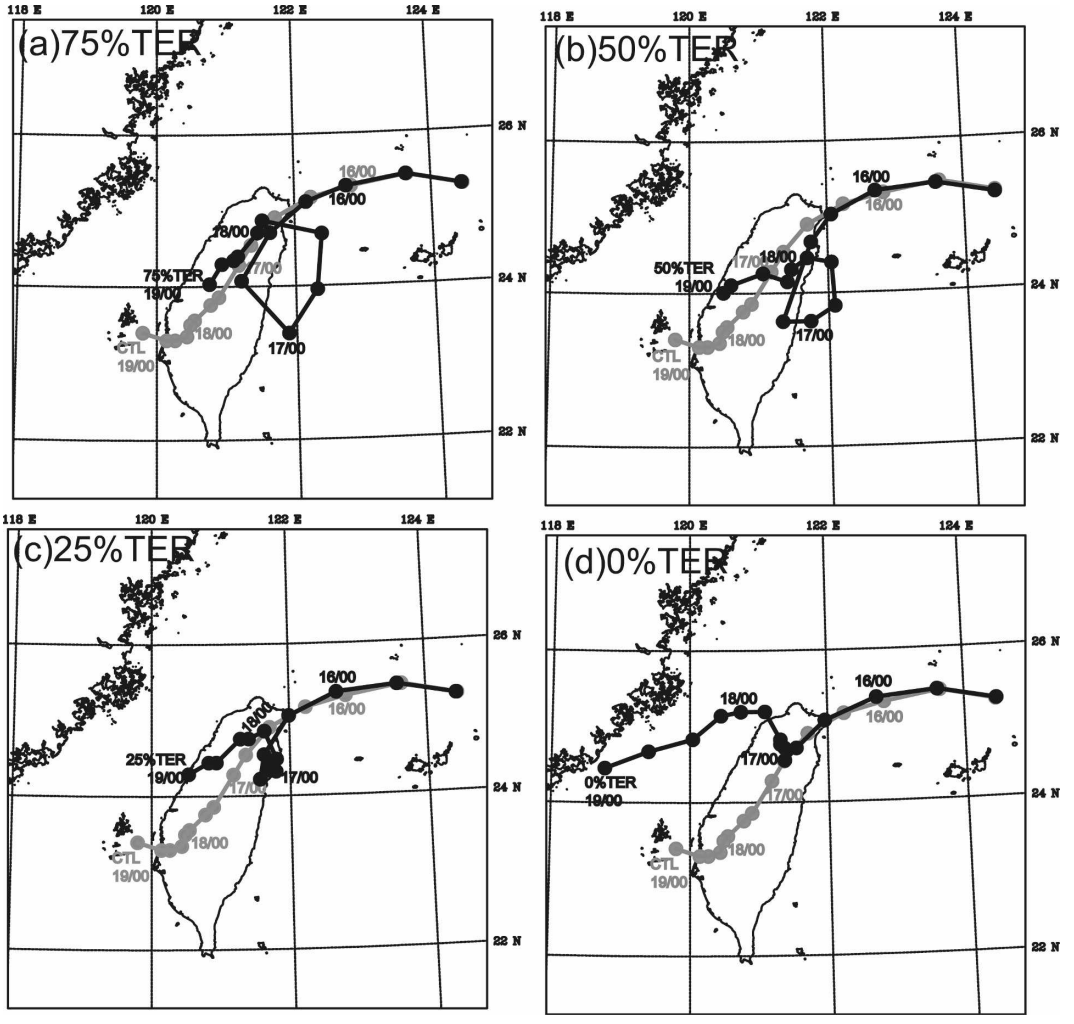

FIG. 18. As in Fig. 4, but from the 84-h sensitivity simulations to reduced terrain heights using (a) 75%, (b) 50%, (c) 25%, and (d) 0% of the terrain (TER) height field in the control run. The control-simulated track (CTL) is also shown.

storms turn around to form a circle between 16/18–30 and 17/18–54, with smaller radii for lower terrain heights. When the topography is completely removed, the simulated storm only dips southwestward on the first day, but it turns northwestward on the second day and then southwestward afterward because of the environmental steering flows (Figs. 3a and 18d). The simulated track of the ocean run closely follows that of the no-terrain run. Based on the sensitivity simulations, it appears that Taiwan's topography tends to slow down Nari's southwestward movement prior to landfall, and the high CMR ridge helps block Nari from passing its peak from the northeast after landfall.

After analyzing the behaviors of the simulated storms, we found that the CMR's blocking effect after Nari's landfall could be understood in terms of the basic-flow Froude number U/NH, where U is the deep-layer across-CMR mean flow, N is the Brunt–Väisälä frequency, and H is the mountain height, following the studies of Lin et al. (2002, 2005, 2006) in which the CMR's deflecting effects on TC tracks are examined. Their results indicate that when U/NH is greater than 0.5 (in addition to the other criteria), the TC track will

TABLE 4. Temporally averaged parameters of terrain-sensitivity experiments during the landfall period (0900–2100 UTC 16 Sep 2001); H is the mountain height, U is the deep-layer across-CMR mean flow, and N is the Brunt–Väisälä frequency (0.01 s^{-1} for all experiments).

Expt	H (m)	U (m s^{-1})	U/NH
CTL	3500	2.10	0.06
75%TER	2625	1.76	0.07
50%TER	1750	1.74	0.10
25%TER	875	0.95	0.11

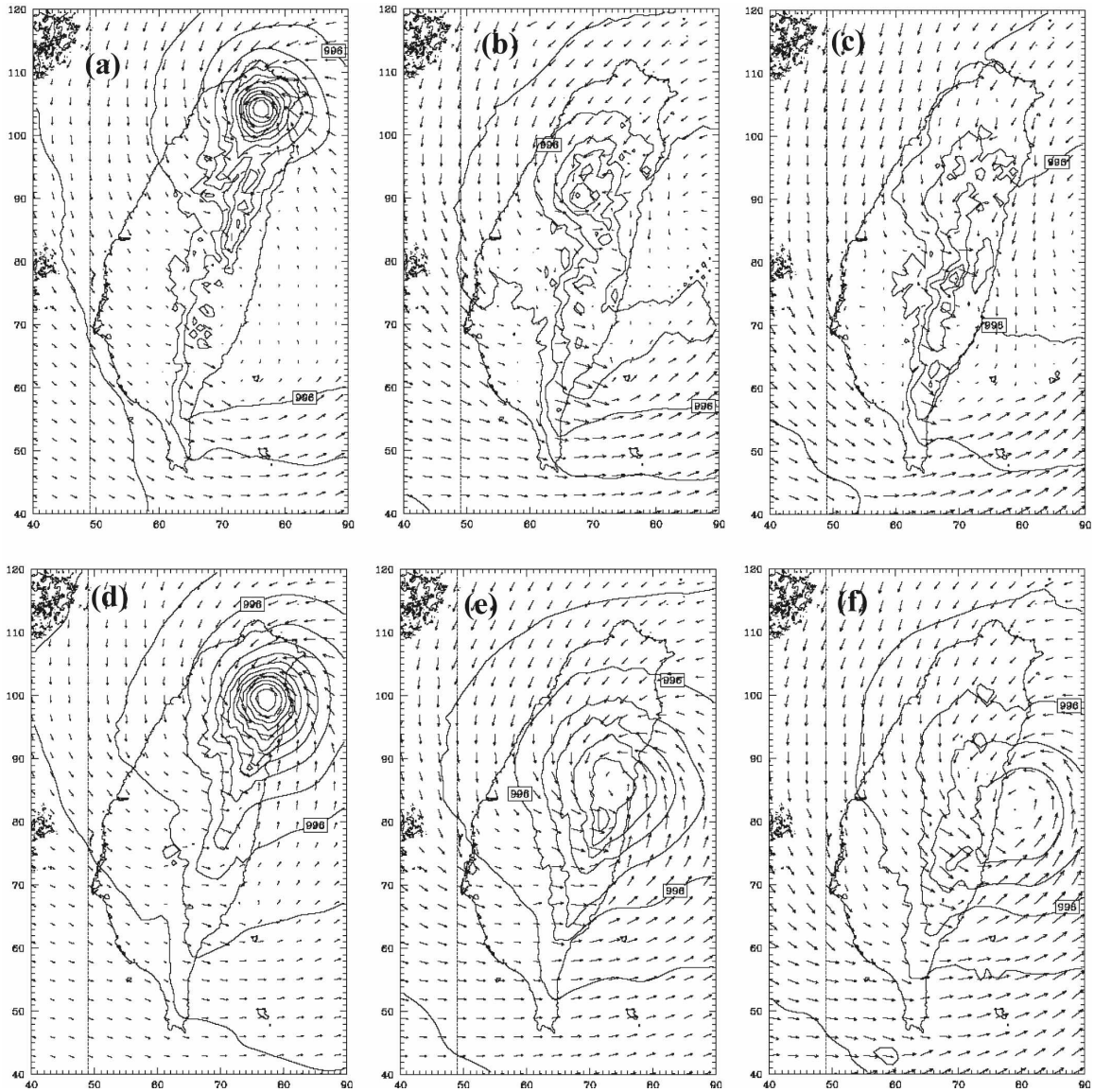

FIG. 19. Near-surface ($\sigma = 0.997$) horizontal wind vectors and sea level isobars (at intervals of 2 hPa) of the CTL run at (a) 1200 UTC 16 Sep, (b) 1800 UTC 16 Sep, and (c) 0000 UTC 17 Sep 2001. (d)–(f) As in (a)–(c), but for the 50%TER run.

be continuous after moving across the CMR. In other words, the track of a slower-moving TC (i.e., smaller *U/NH*), tends to be more "discontinuous" (i.e., deflected) or even could not climb over the mountain.

To quantify the blocking effects of Taiwan's topography, Table 4 shows that for the CTL and three reduced-terrain experiments, the temporally averaged Froude numbers *U*/*NH* during the landfall period are all less than 0.5, yielding "discontinuous" tracks. This implies that the tracks tend to deflect to the left (or eastward) after moving across the CMR, according to Lin et al. (2002, 2005). The CTL track is considered as a special case of "discontinuous" track according to Lin et al. (2005; see their Fig. 12c), because of its smallest value of *U*/*NH* and the replacement of TC vortex by the leeside low after landfall (Fig. 19), resulting in a "straight" CTL path crossing the CMR. Of particular interest is that the other three storms do not continue their eastward tracking afterward, but they begin to turn northward after deflecting to their southern tips and circle to the east of the CMR. An analysis of the large-scale steering flows reveals the importance of the storm–environment interaction in determining the storms' circling tracks (cf. Figs. 18 and 3b). Again, this is because stronger storms of reduced terrain tend to experience a deeper steering layer (Velden and Leslie

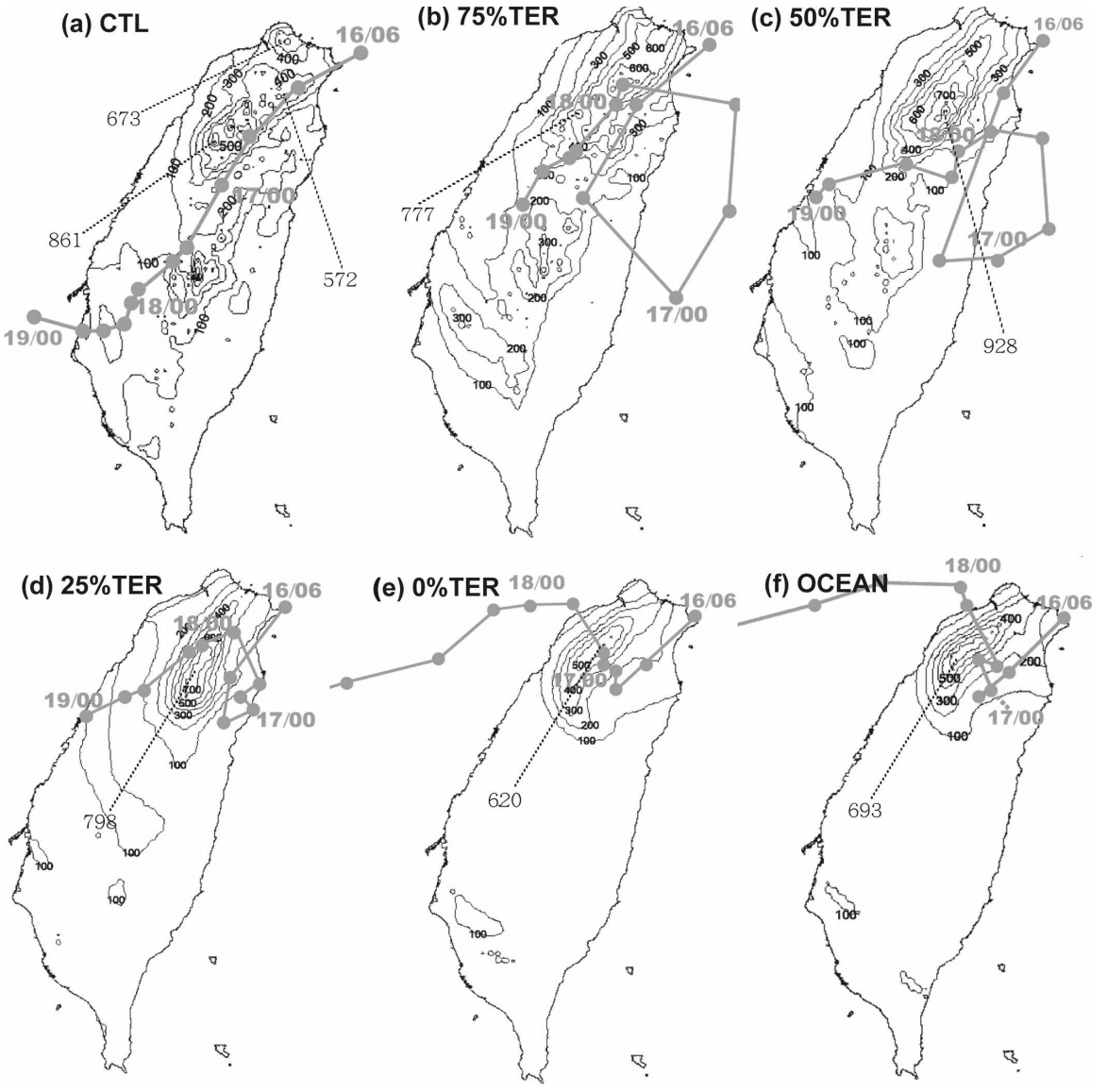

FIG. 20. As in Fig. 6a, but for the 24-h rainfall from (a) the control run, the (b) 75%, (c) 50%, (d) 25%, and (e) 0% terrains, and (f) ocean simulations on 16 Sep 2001. Superposed is the corresponding 6-h track.

1991), which would include the upper-level southwesterly to southerly flows associated with the subtropical high (see Figs. 2d and 3b). For example, the area-averaged steering flows at 16/18–30 appear near-southerly at mid-to-upper levels (σ = 0.325, 0.375, 0.425) for the CTL and reduced-terrain runs (Fig. 3b). This explains well why the circle size of the track becomes smaller, with earlier turning on the lee side, in the sensitivity experiments with lower terrain heights.

b. Accumulated rainfall

In view of the marked directional changes and displacement in the simulated tracks after landfall, it is meaningful to compare only the first 24-h accumulated rainfall from the 6-km grid for these sensitivity simulations. Figure 20 reveals that all the simulations, including the CTL, produce an elongated heavy rainfall pattern over northern Taiwan to the left of the storm tracks. An examination of the area-averaged hodographs shows the significant controlling effects of southwesterly vertical shear vector in the large-scale flow during the first 24 h (cf. Figs. 20 and 21); namely, heavier rainfall tends to occur on the downshear left side of the eyewall (Black et al. 2002; Zhang and Kieu 2006). For the second and third days, the CMR plays a more important role in determining the rainfall distri-

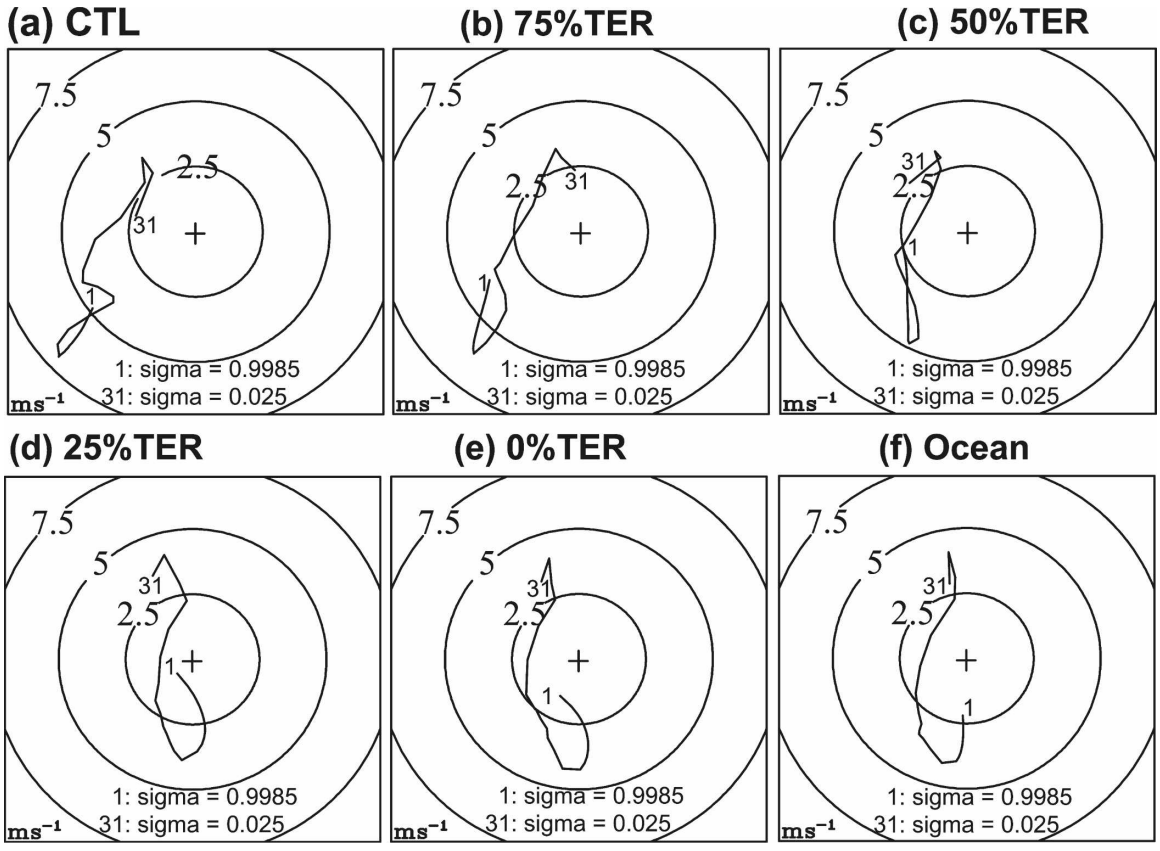

FIG. 21. The hodographs that are obtained by averaging horizontal winds within 200 km from the typhoon center of (a) the control run, the (b) 75%, (c) 50%, (d) 25%, and (e) 0% terrains, and (f) the ocean simulations at 1200 UTC 16 Sep 2001. The circles are at an interval of 2.5 m s^{-1}.

bution on Taiwan than the large-scale sheared flow (see Figs. 6b,c).

It is important to note that higher terrain tends to produce more rainfall on the windward side of the CMR, thus increasing the total accumulated amount. That is, the higher the terrain heights used, the stronger the horizontal moisture flux convergence, and the greater the total accumulated rainfall on Taiwan (Table 5). The slightly more rainfall in the 75% terrain run than in the CTL is caused by the storm's greater residence time over Taiwan on 16 September. However, this enhancement effect is not all linear for local rainfall maxima. For example, the local rainfall maximum is 777 mm in the 75% run (Fig. 20b) but 798 mm in the 25% run (Fig. 20d). With more evaporation from the underlying ocean surface, the ocean run produces slightly more rainfall than the no-terrain run (Table 5 and Figs. 20e,f). The area-averaged 24-h accumulated rainfalls within three different radii (100, 150, and 200 km) from Nari's center are given in Table 6, showing again an expected general trend of decreasing "storm-scale" rainfall with reducing terrain heights over Taiwan.

7. Concluding remarks

In this study, a quadruply nested version of the PSU–NCAR mesoscale model (MM5) with the finest grid size of 2 km is utilized to simulate the track, intensity, kinematic, and precipitation structures of Typhoon Nari (2001). After validating the control simulation

TABLE 5. The percentage of the island-averaged 24-h accumulated rainfall on 16 Sep 2001 from each 6-km sensitivity experiment with respect to the control simulation.

Variable	CTL	75%TER	50%TER	25%TER	0%TER	Ocean
Percentage wrt CTL (%)	100.0	102.9	88.2	70.0	51.9	52.3

TABLE 6. The percentage of the area-averaged 24-h accumulated rainfall within 100-, 150-, and 200-km radii from the typhoon center on 16 Sep 2001 from each 6-km sensitivity experiment with respect to the control simulation.

Radius	No. of points	CTL	75%TER	50%TER	25%TER	0%TER	Ocean
100 km	877	100	97.3	84.2	64.7	62.2	61.5
150 km	1961	100	94.1	85.1	68.5	64.9	64.1
200 km	3503	100	95.4	84.0	71.8	66.3	68.3

against various observations, a series of terrain sensitivity experiments are carried out to examine the effects of Taiwan's topography on Nari's landfalling characteristics.

It is shown that the model reproduces well Nari's track, slow movement, the eye, the eyewall, the spiral rainbands, the basic rainfall pattern, and the local maxima over Taiwan during various landfalling stages, as verified against the best track analyses, radar, and rain gauge observations. In particular, the model captures well the landfall location at 22 h into the integration, albeit 3 h earlier; the rapid filling of central pressure ($\sim$1.67 hPa h^{-1}) and weakening of the maximum surface wind ($\sim$1 m s^{-1} h^{-1}) during the 24-h landfalling period; and the little intensity changes during the subsequent 36 h. The simulated 3-day rainfall totals capture 88% of the observed amount on Taiwan, as well as some local maxima over Mt. Snow and the foothills of the CMR in south central Taiwan.

It is found that Nari's torrential rainfall is determined by the large-scale sheared flows and enhanced by the local topography during the first 24 h after landfall, but it may be more topographically driven afterward. Sensitivity experiments to reduced terrain heights reveal that the impact of Taiwan's terrain on Nari's intensity is linear; that is, higher terrain elevations tend to produce weaker TCs but more accumulated rainfall after landfall. In contrast, reducing the terrain heights produces nonlinear tracks, with circular shapes and variable movements after landfall.

Analyses of the control simulation show that Nari's eyewall and RMW are upright with a larger eye size, and the maximum latent heating is located at the mid to upper troposphere prior to landfall, but the eye shrinks with more clouds filled inward from the eyewall after landfall. In particular, the reflectivity and RMW axes tilt toward Mt. Snow, with the maximum heating located in the lower troposphere. Results show that although the tangential flows are nearly axisymmetric, the radial flows and latent heating profiles are more asymmetric, with pronounced radial outflows above the CMR. Nari's storm intensity remains nearly constant for 36 h after crossing the CMR, indicating that the damping effects by the terrain-induced radial outflows may be balanced by the intensifying effects of strong latent heating associated with the torrential rainfall.

Although the model captures many important landfalling characteristic of Nari, there are still some discrepancies that should be mentioned. For example, the simulated storm appears to propagate at a speed faster than observed prior to landfall, leading to the 3-h earlier time at landfall. The simulated storm appears to be slightly stronger than the observed in terms of radar reflectivity, central pressure, and maximum surface wind. These discrepancies may result from the imperfect initial and boundary conditions, the use of the 2-km grid size (which appears to be still too coarse to explicitly resolve deep convection and turbulence within the inner core), and some uncertainties in cloud microphysics parameterizations.

Nevertheless, the many similarities of the simulated storm to the observed suggest that the model results can be used to further investigate landfalling TC microphysics and thermodynamics, hydrometeor trajectories, and water budgets. All these will be presented in the forthcoming articles in this series of papers.

Acknowledgments. The authors thank Dr. Ron McTaggart-Cowan and two anonymous reviewers for their constructive comments on the manuscript, Prof. Chung-Hsiung Sui for leading the pilot study of Typhoon Nari, Profs. Tai-Chi Chen and Yu-Chieng Liou for the radar data analysis, and Mr. Chi-Hsin Liao for graphics assistance. This research was supported by the National Science Council of Taiwan under Grants NSC 95-2111-M-008-005-AP1, 97-NSPO(B)-SP-FA07-(02)F, and NSC 95-2625-Z-008-003 and by the U.S. National Science Foundation Grant ATM-0342363 and the Office of Navy Research Grant N000140710186.

REFERENCES

Black, M. L., J. F. Gamache, F. D. Marks Jr., C. E. Samsury, and H. E. Willoughby, 2002: Eastern Pacific Hurricanes Jimena of 1991 and Olivia of 1994: The effect of vertical shear on structure and intensity. *Mon. Wea. Rev.,* **130,** 2291–2312.

Braun, S. A., 2006: High-resolution simulation of Hurricane Bonnie (1998). Part II: Water budget. *J. Atmos. Soc.,* **63,** 43–64.

——, and W. Tao, 2000: Sensitivity of high-resolution simulations

of Hurricane Bob (1991) to planetary boundary layer parameterizations. *Mon. Wea. Rev.,* **128,** 3941–3961.

Charney, J. G., 1955: The use of the primitive equations of motion in numerical prediction. *Tellus,* **7,** 22–26.

Chien, F.-C., Y.-H. Kuo, and M.-J. Yang, 2002: Precipitation forecast of MM5 in the Taiwan area during the 1998 Mei-yu season. *Wea. Forecasting,* **17,** 739–754.

Colle, B. A., K. J. Westrick, and C. F. Mass, 1999: Evaluation of MM5 and Eta-10 precipitation forecasts over the Pacific Northwest during the cool season. *Wea. Forecasting,* **14,** 137–154.

Davis, C., and L. F. Bosart, 2001: Numerical simulations of the genesis of Hurricane Diana (1984). Part I: Control simulation. *Mon. Wea. Rev.,* **129,** 1859–1881.

——, and S. Low-Nam, 2001: The NCAR–AFWA tropical cyclone bogussing scheme. U.S. Air Force Weather Agency (AFWA) Rep., 21 pp.

Dudhia, J., 1989: Numerical study of convection observed during the Winter Monsoon Experiment using a mesoscale two-dimensional model. *J. Atmos. Sci.,* **46,** 3077–3107.

——, 1993: A nonhydrostatic version of the Penn State–NCAR mesoscale model: Validation tests and simulation of an Atlantic cyclone and cold front. *Mon. Wea. Rev.,* **121,** 1493–1513.

Fovell, R. G., and Y. Ogura, 1988: Numerical simulation of a midlatitude squall line in two dimensions. *J. Atmos. Sci.,* **45,** 3846–3879.

Grell, G. A., 1993: Prognostic evaluation of assumptions used by cumulus parameterizations. *Mon. Wea. Rev.,* **121,** 764–787.

——, J. Dudhia, and D. R. Stauffer, 1994: A description of the fifth-generation Penn State/NCAR Mesoscale Model (MM5). NCAR Tech. Note NCAR/TN-398+STR, 121 pp.

Holton, J. R., 2004: *An Introduction to Dynamical Meteorology*. 4th ed. Academic Press, 535 pp.

Hong, S.-Y., and H.-L. Pan, 1996: Nocturnal boundary layer vertical diffusion in a medium-range forecast model. *Mon. Wea. Rev.,* **124,** 2322–2339.

Houze, R. A., Jr., F. D. Marks Jr., and R. A. Black, 1992: Dual-aircraft investigation of the inner core of Hurricane Norbert. Part II: Mesoscale distribution of ice particles. *J. Atmos. Sci.,* **49,** 943–962.

Huang, C.-Y., Y.-H. Kuo, S.-H. Chen, and F. Vandenberghe, 2005: Improvements in typhoon forecasts with assimilated GPS occultation refractivity. *Wea. Forecasting,* **20,** 931–953.

Jorgensen, D. P., 1984: Mesoscale and convective-scale characteristics of mature Hurricanes. Part II: Inner core structure of Hurricane Allen (1980). *J. Atmos. Sci.,* **41,** 1287–1311.

Kurihara, Y., and M. A. Bender, 1982: Structure and analysis of the eye of a numerically simulated tropical cyclone. *J. Meteor. Soc. Japan,* **60,** 381–395.

Li, M.-H., M.-J. Yang, R. Soong, and H.-L. Huang, 2005: Simulating typhoon floods with gauge data and mesoscale-modeled rainfall in a mountainous watershed. *J. Hydrometeor.,* **6,** 306–323.

Lin, Y.-L., D. B. Ensley, S. Chiao, and C.-Y. Huang, 2002: Orographic influences on rainfall and track deflection associated with the passage of a tropical cyclone. *Mon. Wea. Rev.,* **130,** 2929–2950.

——, S.-Y. Chen, C. M. Hill, and C.-Y. Huang, 2005: Control parameters for the influence of a mesoscale mountain range on cyclone track continuity and deflection. *J. Atmos. Sci.,* **62,** 1849–1866.

——, N. C. Witcraft, and Y.-H. Kuo, 2006: Dynamics of track deflection associated with the passage of tropical cyclones over a mesoscale mountain. *Mon. Wea. Rev.,* **134,** 3509–3538.

Liu, Y., D.-L. Zhang, and M. K. Yau, 1997: A multiscale numerical study of Hurricane Andrew (1992). Part I: Explicit simulation and verification. *Mon. Wea. Rev.,* **125,** 3073–3093.

——, ——, and ——, 1999: A multiscale numerical study of hurricane Andrew (1992). Part II: Kinematics and inner-core structures. *Mon. Wea. Rev.,* **127,** 2597–2616.

Marks, F. D., Jr., and R. A. Houze Jr., 1987: Inner core structure of Hurricane Alicia from airborne Doppler radar observations. *J. Atmos. Sci.,* **44,** 1296–1317.

McAdie, C. J., and M. B. Lawrence, 2000: Improvements in tropical cyclone track forecasting in the Atlantic basin, 1978–99. *Bull. Amer. Meteor. Soc.,* **81,** 989–997.

Medina, S., and R. A. Houze Jr., 2003: Air motions and precipitation growth in Alpine storms. *Quart. J. Roy. Meteor. Soc.,* **129,** 345–371.

Reisner, J., R. J. Rasmussen, and R. T. Bruitjes, 1998: Explicit forecasting of supercooled liquid water in winter storms using the MM5 mesoscale model. *Quart. J. Roy. Meteor. Soc.,* **124,** 1071–1107.

Rogers, R., S. Chen, J. Tenerelli, and H. Willoughby, 2003: A numerical study of the impact of vertical shear on the distribution of rainfall in Hurricane Bonnie (1998). *Mon. Wea. Rev.,* **131,** 1577–1599.

Simpson, R. H., 1974: The hurricane disaster-potential scale. *Weatherwise,* **27,** 169.

Sui, C.-H., and Coauthors, 2002: Meteorology–hydrology study targets Typhoon Nari and Taipei flood. *Eos, Trans. Amer. Geophys. Union,* **83,** 265–270.

——, X. Li, M.-J. Yang, and H.-L. Huang, 2005: Estimation of oceanic precipitation efficiency in cloud models. *J. Atmos. Sci.,* **62,** 4358–4370.

Tuleya, R. E., 1994: Tropical storm development and decay: Sensitivity to surface boundary conditions. *Mon. Wea. Rev.,* **122,** 291–304.

Velden, C. S., and L. M. Leslie, 1991: The basic relationship between tropical cyclone intensity and the depth of the environmental steering layer in the Australian region. *Wea. Forecasting,* **6,** 244–253.

Warner, T. T., and H. M. Hsu, 2000: Nested-model simulation of moist convection: The impact of coarse-grid parameterized convection on fine-grid resolved convection. *Mon. Wea. Rev.,* **128,** 2211–2231.

Willoughby, H. E., H.-L. Jin, S. J. Lord, and J. M. Piotrowicz, 1984a: Hurricane structure and evolution as simulated by an axisymmetric, nonhydrostatic numerical model. *J. Atmos. Sci.,* **41,** 1169–1186.

——, F. D. Marks Jr., and R. J. Feinberg, 1984b: Stationary and moving convective bands in hurricanes. *J. Atmos. Sci.,* **41,** 3189–3211.

Wu, C.-C., T.-H. Yen, Y.-H. Kuo, and W. Wang, 2002: Rainfall simulation associated with Typhoon Herb (1996) near Taiwan. Part I: The topographic effect. *Wea. Forecasting,* **17,** 1001–1015.

Yang, M.-J., B. J.-D. Jou, S.-C. Wang, J.-S. Hong, P.-L. Lin, J.-H. Teng, and H.-C. Lin, 2004: Ensemble prediction of rainfall during the 2000–2002 Mei-Yu seasons: Evaluation over the Taiwan area. *J. Geophys. Res.,* **109,** D18203, doi:10.1029/2003JD004368.

Yau, M. K., Y. Liu, D.-L. Zhang, and Y. Chen, 2004: A multiscale numerical study of Hurricane Andrew (1992). Part VI: Small-

scale inner-core structures and wind streaks. *Mon. Wea. Rev.,* **132,** 1410–1433.

Zhang, D.-L., and C. Q. Kieu, 2006: Potential vorticity diagnosis of a simulated hurricane. Part II: Quasi-balanced contributions to forced secondary circulations. *J. Atmos. Sci.,* **63,** 2898–2914.

——, Y. Liu, and M. K. Yau, 2000: A multiscale numerical study of hurricane Andrew (1992). Part III: Dynamically induced vertical motion. *Mon. Wea. Rev.,* **128,** 3772–3788.

—— ——, and ——, 2001: A multiscale numerical study of Hurricane Andrew (1992). Part IV: Unbalanced flows. *Mon. Wea. Rev.,* **129,** 92–107.

——, ——, and ——, 2002: A multiscale numerical study of Hurricane Andrew (1992). Part V: Inner-core thermodynamics. *Mon. Wea. Rev.,* **130,** 2745–2763.

Zhu, T., D.-L. Zhang, and F. Weng, 2004: Numerical simulation of Hurricane Bonnie (1998). Part I: Eyewall evolution and intensity changes. *Mon. Wea. Rev.,* **132,** 225–241.